Available online at www.sciencedirect.com
ScienceDirect
Journal of Computational Physics 225 (2007) 2175–2197
JOURNAL OF COMPUTATIONAL PHYSICS
www.elsevier.com/locate/jcp

# Initial-value approach to study the inertio-gravity waves without the 'traditional approximation'

Akira Kasahara *

*National Center for Atmospheric Research, Boulder, CO 80307, USA*

Received 5 December 2006; received in revised form 5 March 2007; accepted 6 March 2007
Available online 21 March 2007

**Abstract**

An initial-value problem is formulated with linear Boussinesq equations to study the inertio-gravity waves without the ''traditional approximation'' that is to include a complete effect of rotation. Motions are assumed to be horizontally periodic, but bounded vertically at the top and bottom. The evolution of the vertical structure of wave motions can be calculated from given initial conditions with a one-dimensional finite-difference version of the model with or without forcing/dissipation under a variable thermal buoyancy condition in height.

This program is intended to use as a simple numerical laboratory to study the time-evolution of inertio-gravity waves. Examples show for (1) the free oscillations using the normal mode solutions as initial conditions, and (2) the forced oscillations as a simulation of near-inertial currents in the oceans generated by atmospheric storms. An emphasis is made to asses the role of the horizontal component of the earth's rotation which has been traditionally neglected in the study of inertio-gravity waves.


*Keywords:* Inertio-gravity waves; Normal modes of oscillations; Traditional approximation; Boundary-induced inertial mode

## 1. Introduction

One objective of this work is to contribute to understanding the nature of so-called 'traditional approximation' which has been adopted in modeling of the atmosphere and ocean. In this approximation dynamical terms related to the horizontal component of the Coriolis vector, $2\Omega\cos\phi$, where $\Omega$ denotes the angular velocity of rotation and $\phi$ is latitude, are neglected. This particular terminology apparently first introduced by Eckart [8, p. 95], but the question of justification on this approximation has been around much longer in the literature of meteorology. For example, when Richardson [29, p. 33] formulated a scheme of weather prediction by numerical process, he pondered on this question, since these terms are much smaller than the rest. Nevertheless, not finding any good reason to discard, he decided to keep one of them. A rational for discarding these terms was discussed by Phillips [24] for the motions of a shallow atmosphere. Namely, when the assumption that the depth of atmosphere is small compared with the radius of the earth is applied

* Present address: National Center for Atmospheric Research, 1850 Table Mesa Drive, Boulder, CO 80305, USA.
*E-mail address:* kasahara@ucar.edu

0021-9991/$ - see front matter © 2007 Elsevier Inc. All rights reserved.
doi:10.1016/j.jcp.2007.03.006

systematically to the equations of motion on a rotating sphere, the traditional approximation should be adopted in order to strictly conserve angular momentum as a desirable feature in the numerical integration of the equations of motion. Phillips [26, p. 8] also analyzed the frequency equation of internal waves involving the $\cos\phi$ Coriolis terms and concluded that the dynamical effect of these terms can be neglected when the ratio between $\Omega$ and buoyancy frequency $N$ is very small. However, Phillips [25] cautioned that the non-traditional effect may enter significantly in the finer details of ''inertia waves''.

A renewed interest in questioning the consequence of the traditional approximation arose in the last 10 years or so due to an effort to improve modeling of the atmosphere and ocean in the context of long-term climate simulation with global circulation models as one is concerned with such minute effect of increasing greenhouse gases in the atmosphere. Based on the scale analysis of global circulation model, White and Bromley [38] suggested that the $\cos\phi$ Coriolis terms may attain magnitudes of order 10% of those key terms in the hydrostatic primitive equations. However, it is fair to state that no conclusive experience has been reported to support the immediate urgency to discard the primitive-equation formulation in favor of more advanced modeling [39]. Nevertheless, some modeling groups such as the UK Met Office went forward to develop an advanced dynamical core of multi-scale weather and climate model without shallowness and traditional approximations in the Eulerian equations of motion [6].

Oceanographers have also been concerned about the consequence of traditional approximation as reflected in the discussion by Veronis [36] and subsequent studies on the role of the $\cos\phi$ Coriolis terms. Ocean currents are greatly influenced by mechanical forcing of storms and tides. Oscillating currents with near-inertial frequency (clockwise in northern hemisphere at a rate of $2\Omega\sin\phi$ revolutions per day) are one of the most prominent features in the sea [23]. Therefore, oceanographers have much more interest in ageostrophic motions such as inertio-gravity waves and prefer that more efforts are put into understand the physics of non-traditional effects [11].

The approach so far to elucidate the role of the $\cos\phi$ Coriolis terms is mostly based on the wave frequency analysis treating as an eigenvalue problem (see Refs. in [35,14,15,11]). However, a direct numerical simulation approach is another option. Marshall et al. [21] designed a comprehensive ocean model based on the incompressible Navier–Stokes equations in spherical geometry without the traditional approximation. Their results from preliminary numerical experiments indicate that the impact of the non-traditional effects in horizontal currents in ocean gyres is very small. This is understandable, because the non-traditional effects affect mostly on near-inertial motions and their energy contribution to large-scale horizontal currents is rather small in a relatively short time span.

More specific numerical experiments for detecting the non-traditional effects were designed by Beckmann and Diebels [1] using a linear Cartesian incompressible primitive-equation ocean model including the complete rotation terms. The results of their experiments clearly indicate rather subtle differences between the runs with and without the $\cos\phi$ Coriolis terms. Although their experiments were carried out using theoretical consideration as a guide, no direct comparison between the theory and the experiment was attempted. It seems desirable to design still simpler numerical experiments from which we can learn a rather unfamiliar role of the non-traditional effects in the inertio-gravity waves by combining both the initial-value and eigenvalue approaches.

This work is an extension of [17] which calculated the normal modes of linear Boussinesq model with the non-traditional effects in Cartesian geometry as a matrix eigenvalue problem. In this work the solutions of the same problem will be examined by using the initial-value method. The basic equations used here are described in Section 2. The normal mode solutions of the basic equations for a constant $N$, that will be used to examine the numerical solutions from the initial-value approach, are reviewed in Section 3. The numerical finite-difference formulation of the initial-value problem is discussed in Section 4 and the numerical results are presented in Section 5. The conclusions and additional comments are stated in Section 6.

## 2. Formulation of the problem

### 2.1. Basic equations

The basic equations are identical to those in [17], except that we now include additional forcing/dissipation effects to study forced problems as well. The model consists of linear Boussinesq equations in the

horizontally unbounded and vertically stratified domain of uniform depth $H_s$ with Cartesian coordinates $(x, y, z, t)$ on tangent plane. Here $x$, $y$, and $z$ are directed eastward, northward, and upward respectively, and $t$ denotes time. The dependent variables are the velocity components $(u, v, w)$ corresponding to $(x, y, z)$ together with $p$ and $s$ which are the perturbation pressure divided by constant volume mean density and the buoyancy, respectively. The basic equations are expressed in dimensionless form using the scaling parameters presented in Appendix. Unless mentioned otherwise, all variables and parameters in this article are expressed in dimensionless form. The dependent variables are complex numbers, but the parameters are real numbers.

The basic equations are

$$\frac{\partial u}{\partial t} - fv + a_s \tilde{f} w + \frac{\partial p}{\partial x} = \frac{\partial F_x}{\partial z}, \tag{2.1}$$

$$\frac{\partial v}{\partial t} + fu + \frac{\partial p}{\partial y} = \frac{\partial F_y}{\partial z}, \tag{2.2}$$

$$\frac{\partial w}{\partial t} - a_s^{-1} \tilde{f} u - s + a_s^{-2} \frac{\partial p}{\partial z} = 0, \tag{2.3}$$

$$\frac{\partial u}{\partial x} + \frac{\partial v}{\partial y} + \frac{\partial w}{\partial z} = 0, \tag{2.4}$$

$$N^{-2} \frac{\partial s}{\partial t} + w = 0. \tag{2.5}$$

The vertical and horizontal components, respectively, of Coriolis vector are defined by

$$f = \sin\phi \quad \text{and} \quad \tilde{f} = \cos\phi, \tag{2.6}$$

where $\phi$ denotes the latitude of coordinate center. Also, $N(z)$ denotes Brunt–Väisälä frequency, and $a_s$ stands for the aspect ratio defined by

$$a_s = H_s L_s^{-1}, \tag{2.7}$$

where $H_s$ and $L_s$ are the vertical and horizontal scales of the domain, respectively. See Appendix.

Quantities $F_x$ and $F_y$ represent the vertical flux of specific momentum in $(x, y)$-directions, respectively, and are expressed by

$$F_x = K(z) \frac{\partial u}{\partial z} \quad \text{and} \quad F_y = K(z) \frac{\partial v}{\partial z}, \tag{2.8}$$

where $K(z)$ denote the coefficient of eddy diffusivity as a function of height.

### 2.2. Boundary conditions and energy equation

We solve Eqs. (2.1)–(2.5) as an initial-value problem with the boundary conditions that the horizontal domain is periodic in $x$ and $y$. The vertical domain is bounded by the bottom at $z = 0$ and the top at $z = 1$, where we assume that

$$w(x, y, 0, t) = w(x, y, 1, t) = 0. \tag{2.9}$$

We also assume that the momentum fluxes (stresses) are specified at the top and bottom as

$$\begin{aligned} &F_x = F_{xs} \quad \text{and} \quad F_y = F_{ys} \quad \text{at } z = 1, \\ &F_x = F_y = 0 \quad \text{at } z = 0. \end{aligned} \tag{2.10}$$

We multiply Eqs. (2.1)–(2.5) by the complex conjugate variables, $u^*, v^*, w^*, p^*, s^*$, respectively. Also, we create another set of the complex conjugate forms of Eqs. (2.1)–(2.5) and multiply them by the variables $u, v, w, p, s$, respectively. We then add the two resulting sets together and integrate the sum with respect to $x$, $y$ and $z$ in the three-dimensional space using the above boundary conditions. The result is the following energy equation in the form:

$$\frac{\partial}{\partial t}\int_0^1\int_0^{2\pi}\int_0^{2\pi}(TE)\,\mathrm{d}x\,\mathrm{d}y\,\mathrm{d}z=\int_0^1\int_0^{2\pi}\int_0^{2\pi}DF\,\mathrm{d}x\,\mathrm{d}y\,\mathrm{d}z, \tag{2.11}$$

where the total energy product $TE$ is defined by

$$TE=|u|^2+|v|^2+a_s^2|w|^2+N^{-2}a_s^2|s|^2. \tag{2.12}$$

The right-hand side of (2.11) is the time-rate of energy change due to dissipation/forcing and the term $DF$ is the work done by frictional force defined by

$$DF=u^*\frac{\partial F_x}{\partial z}+u\frac{\partial F_x^*}{\partial z}+v^*\frac{\partial F_y}{\partial z}+v\frac{\partial F_y^*}{\partial z}. \tag{2.13}$$

### 2.3. Vertical structure equations

The parameters in Eqs. (2.1)–(2.5) are independent of the horizontal coordinates. Also, horizontal boundary conditions are periodic. Therefore, we can express their solutions in the form

$$(u,v,w,p,s)=(U,\mathrm{i}V,\mathrm{i}W,P,S)\exp[\mathrm{i}(mx+ny)], \tag{2.14}$$

where $\mathrm{i}=\sqrt{-1}$, $m$ and $n$ are the dimensionless wavenumbers in the $x$ and $y$ directions

$$m=2\pi L_s L_x^{-1},\quad n=2\pi L_s L_y^{-1}. \tag{2.15}$$

Here, $L_x$ and $L_y$ are the wavelengths in the $x$ and $y$ directions, respectively. The coefficients $U,V,W,P$, and $S$ are the complex numbers and functions of $z$ and $t$ only. The imaginary factor i in front of $V$ and $W$ are introduced for convenience to take care of the phase differences of $V$ and $W$ relative to other variables as done in earlier studies.

Similarly, we express the momentum fluxes as harmonic functions in $x$ and $y$ directions as

$$(F_x,F_y)=(\widehat{F}_x,\mathrm{i}\widehat{F}_y)\exp[\mathrm{i}(mx+ny)]. \tag{2.16}$$

By substituting the expressions (2.14) and (2.16) into Eqs. (2.1)–(2.5), we can factor out the horizontally dependent harmonic terms and obtain the following vertical structure equations for complex variables $U,V,W,P$, and $S$ which are functions of $t$ and $z$.

$$\frac{\partial U}{\partial t}-\mathrm{i}fV+\mathrm{i}a_s\tilde{f}W+\mathrm{i}mP=\frac{\partial\widehat{F}_x}{\partial z}, \tag{2.17}$$

$$\frac{\partial V}{\partial t}-\mathrm{i}fU+nP=\frac{\partial\widehat{F}_y}{\partial z}, \tag{2.18}$$

$$\frac{\partial W}{\partial t}+\mathrm{i}a_s^{-1}\tilde{f}U+\mathrm{i}S-\mathrm{i}a_s^{-2}\frac{\partial P}{\partial z}=0, \tag{2.19}$$

$$\mathrm{i}mU-nV+\mathrm{i}\frac{\partial W}{\partial z}=0, \tag{2.20}$$

$$N^{-2}\frac{\partial S}{\partial t}+\mathrm{i}W=0. \tag{2.21}$$

There is no prognostic equation for $P$ in the above system and it must be determined diagnostically to satisfy the incompressibility condition (2.20) for all time. The diagnostic equation for $P$ is derived by first taking the derivative of (2.20) with respect to $t$ and then eliminating the time tendencies of $U,V$, and $W$ using their corresponding prognostic equations. The result is

$$(m^2+n^2)P-a_s^{-2}\frac{\partial^2P}{\partial z^2}=mfV-a_s m\tilde{f}W+\mathrm{i}fnU-\frac{\partial S}{\partial z}-a_s^{-1}\tilde{f}\frac{\partial U}{\partial z}-\mathrm{i}m\frac{\partial\widehat{F}_x}{\partial z}+n\frac{\partial\widehat{F}_y}{\partial z}. \tag{2.22}$$

In order to solve (2.17)–(2.22) as an initial-value problem, we need the boundary conditions as well as initial conditions. From (2.9), we have $W=0$ at $z=0$ and 1. Thus, from (2.21) the time tendency of $S$ at the boundaries should be zero. Since we will assume that $S$ is zero there initially, $S$ remains zero at the boundaries. To solve Poisson's equation (2.22), we need boundary conditions. Since $W=S=0$ there, from (2.19) we derive the following Neumann conditions on $P$,

$$\frac{\partial P}{\partial z} = a_s \tilde{f} U \quad \text{at } z = 0 \text{ and } 1. \tag{2.23}$$

Knowing the initial conditions for $U, V, W$, and $S$, we can determine $P$ from (2.22) with (2.23). The same process will be repeated to update all the variables at any later time.

Before we describe the method of time integration of this system, it is instructive to review the general solutions of the inviscid case by setting the right-hand sides of (2.17) and (2.18) to zero.

## 3. Normal mode solutions of the free oscillations

In the case of constant buoyancy parameter $N = N_0$, the solutions of inviscid case that satisfy the boundary conditions (2.9) are expressed in analytical form. The eigensolutions have been discussed by many investigators in various forms [8,32,20,33,2,22,35,14,15,17,7,11]. Here, we summarize only the pertinent aspects of the eigensolutions as given in [17]. The eignsolutions are periodic in time with the frequency $\sigma$. The eigenfunctions of the vertically dependent parts are expressed by the same notation as in Section 2 with the addition of overbar.

The solutions of $\overline{W}$ and $\overline{P}$ are given by

$$\overline{W} = A \sin(kz) \exp[\mathrm{i}(a_s \Gamma_2 z - \sigma t)], \tag{3.1}$$

$$\overline{P} = A(m^2 + n^2)^{-1} [k\sigma^{-1}(f^2 - \sigma^2)\cos(kz) - a_s \tilde{f} m \sin(kz)] \exp[\mathrm{i}(a_s \Gamma_2 z - \sigma t)], \tag{3.2}$$

where $A$ denotes a real coefficient as given later, and $k$ is the half-vertical wavenumber defined by

$$k = k_i \pi \tag{3.3}$$

with $k_i = 1, 2, \ldots$ denote the vertical mode index. The factor $\Gamma_2$ is rather unique to the problem involving $\tilde{f}$ and is defined by

$$\Gamma_2 = \frac{-nf\tilde{f}}{(f^2 - \sigma^2)}. \tag{3.4}$$

Note that the magnitude of $\Gamma_2$ becomes large when the frequency $\sigma$ approaches to the Coriolis frequency $f$ and has a profound influence on the character of near-inertial eigenfunctions. This was first noticed by Eckart [8, see p. 134] and later by many investigators mentioned earlier.

Once the functions $\overline{W}$ and $\overline{P}$ are determined, the functions $\overline{U}, \overline{V}$ and $\bar{S}$ are calculated from the following expressions:

$$\overline{U} = -(f^2 - \sigma^2)^{-1} [(\sigma m + \mathrm{i} f n)\overline{P} + a_s \sigma \tilde{f} \overline{W}], \tag{3.5}$$

$$\overline{V} = (f^2 - \sigma^2)^{-1} [(f m + \mathrm{i}\sigma n)\overline{P} + a_s f \tilde{f} \overline{W}], \tag{3.6}$$

$$\overline{S} = \sigma^{-1} N_0^2 \overline{W}. \tag{3.7}$$

The coefficient of eigenfunctions, $A$, is obtained by the normalization of the eigenfunctions as discussed in [17]. Here, we only present the result:

$$A^{-2} = \frac{(f^2 + \sigma^2)}{2(f^2 - \sigma^2)^2 + (m^2 + n^2)} \left[ \frac{(f^2 - \sigma^2)^2 k^2}{\sigma^2} + a_s^2 \tilde{f}^2 n^2 \right] + \frac{1}{2} a_s^2 \left( 1 + \frac{N_0^2}{\sigma^2} \right). \tag{3.8}$$

The eigenfunctions require the eigenfrequency $\sigma$ to satisfy the following dispersion equation,

$$(m^2 + n^2 + a_s^{-2} k^2)\sigma^4 - [(m^2 + n^2)(N_0^2 + f^2) + n^2 \tilde{f}^2 + 2a_s^{-2} k^2 f^2]\sigma^2 + [(m^2 + n^2) N_0^2 + a_s^{-2} k^2 f^2] f^2 = 0. \tag{3.9}$$

This is a quadratic equation in $\sigma^2$. Therefore, there are two kinds of wave oscillations which propagate horizontally in opposite directions with the same phase speed. When $N_0 > f$, the first kind has $\sigma$ larger than $f$ and it has the same property of the traditional inertio-gravity waves, but the eigensolutions are slightly modified by the presence of $\tilde{f}$. This is referred here to the inertio-gravity (IG) mode. The second kind has $\sigma$ less than $f$

which emerges under the non-traditional condition in a vertically bounded domain. We will refer this kind to the boundary-induced inertial (BII) mode. While the possibility of this kind of waves has been known in the past, a peculiar nature of the eigensolutions has only recently been explored [35,14,15,7,11,17]. The peculiarity of the eigenfunctions comes from the factor $\exp(\mathrm{i}a_s\Gamma_2 z)$ due to the fact that, when the inviscid version of Eqs. (2.1)–(2.5) are reduced to a single equation for only $w$, a mixed derivative term of $w$ with respect to $y$ and $z$ appears [32,2,11]. Its argument $a_s\Gamma_2$ become rather large when $\sigma$ approaches to $f$. Hence, the vertical profiles of eigenfunctions may become highly variable. Of course, the aspect ratio of wave motions $a_s$ is important too and the smallness of $a_s$ can compensate the largeness of $\Gamma_2$ for near-inertial motions.

It is clear that the non-traditional nature of inertio-gravity waves can be quite different from what we know of the traditional view when the frequency $\sigma$ approaches to $f$. However, knowledge on the properties of normal modes does not directly translate into our understanding of the motions generated by external causes as the projections of external forcing onto the normal modes are required. Next, we will investigate the response of the model to some external forces as an initial-value problem using the finite-difference time integration method.

## 4. Solutions of Eqs. (2.17)–(2.21) by a time integration scheme

### 4.1. Finite-difference grid layout

We set up a two-dimensional grid with increments $\Delta t$ in time and $\Delta z$ in the vertical domain, bounded by $z = 0$ and 1. We express a grid point by $z_j = j\Delta z$ and $t_l = l\Delta t$, where $j$ is an integer from 0 at the bottom to $J$ at the top and $l$ is also an integer from the initial time 0 onward. Fig. 1 shows the vertical grid of equal increment $\Delta z = 1/J$. Variables $W_j^l$ and $S_j^l$ are placed at an integer level $j$ (top and bottom of cell). Variables $U_j^l, V_j^l$ and $P_j^l$ are at a half-integer level $j + 1/2$ (mid-point of cell). Parameters $N(j\Delta z) = N_j$ and $K(j\Delta z) = K_j$ are placed at the integer levels same as $W$ and $S$. Similarly, flux $\widehat{F}_x$ and $\widehat{F}_y$ are given at the integer levels $j$. To avoid an overburden of subscript and superscript notation, their use will be omitted as long as confusion does not arise.

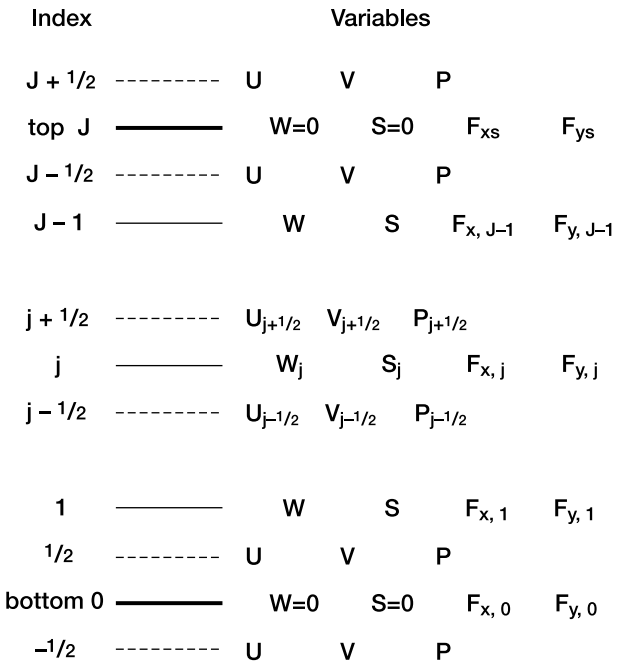


Fig. 1. Vertical grid with uniform increment $\Delta z$. Solid lines for integer level and dashed lines for half-integer levels.

### 4.2. Boundary conditions

Because the vertical derivative of $u$ or $v$ is involved in calculating $F_x$ or $F_y$ as seen in (2.8), it is convenient to add additional half-integer levels, $J+1/2$ outside the top and $-1/2$ below the bottom. By combining (2.8) and (2.10), we then get

$$\begin{aligned} &U_{J+1/2} = U_{J-1/2} + \left(\frac{\Delta z}{K}\right)\widehat{F}_{xs} \quad \text{at } z = 1, \\ &U_{-1/2} = U_{1/2} \quad \text{at } z = 0. \end{aligned} \tag{4.1}$$

We similarly define the variable $V_{J+1/2}$ and $V_{-1/2}$.

To solve the difference form of Poisson's equation (2.22) on this grid, it is necessary to have the values of $P_{J+1/2}$ and $P_{-1/2}$ which can be obtained from the difference form of (2.23) as

$$\begin{aligned} &P_{J+1/2} = P_{J-1/2} + 0.5 a_s \tilde{f} \Delta z (U_{J+1/2} + U_{J-1/2}), \\ &P_{-1/2} = P_{1/2} - 0.5 a_s \tilde{f} \Delta z (U_{1/2} + U_{-1/2}). \end{aligned} \tag{4.2}$$

### 4.3. Time integration scheme

We define the following vector $\mathbf{Y}$ at time level $l$, whose elements consist of the values of $W$ and $S$ at integer levels and the values of $U, V$ and $P$ all at half-integer levels.

$$\begin{aligned} \mathbf{Y}(l) = (&U_{-1/2}, U_{1/2}, \ldots U_{J-1/2}, U_{J+1/2}, V_{-1/2}, V_{1/2}, \ldots V_{J-1/2}, V_{J+1/2}, P_{-1/2}, P_{1/2}, \ldots P_{J-1/2}, P_{J+1/2}, \\ &W_0, W_1, \ldots W_{J-1}, W_J, S_0, S_1, \ldots S_{J-1}, S_J)^{\mathrm{T}}. \end{aligned} \tag{4.3}$$

Similarly, we define the flux vector $\mathbf{F}(l)$ whose elements consist of values of $\widehat{F}_x$ and $\widehat{F}_y$ at integer levels.

We then construct the difference form of the system (2.17)–(2.22) by approximating the derivatives with respect $z$ by centered differences and the variables, which are not available at particular levels, by the arithmetic averages of nearby variables at a particular level. The result can be represented symbolically by

$$\frac{\Delta \mathbf{Y}}{\Delta t} = \mathbf{L}(\mathbf{Y}(l), \mathbf{F}(l)), \tag{4.4}$$

where $\Delta \mathbf{Y} = \mathbf{Y}(l+1) - \mathbf{Y}(l)$ and $\mathbf{L}$ denotes the difference operator constructed using the values of its argument at time level $l$. The time integration of (4.4) is carried out by the fourth order Runge–Kutta method starting from the initial condition $\mathbf{Y}(0)$ with a specification of $\mathbf{F}(l)$.

We should comment on the use of complex arithmetic in this problem. If the traditional approximation were adopted, it is not necessary to solve Eq. (4.4) with complex arithmetic, because the problem becomes independent in the horizontal and vertical directions. However, this is not the case here. There are two coupled systems for the real and imaginary parts of (4.4). They must be solved simultaneously.

Whenever the prognostic variables are calculated at each fractional time step during one $\Delta t$ iteration, the diagnostic variable $P$ must be obtained also by solving the difference form of one-dimensional Poisson's equation (2.22) with the boundary conditions (4.2). This is done by using the method described by Richtmyer and Morton [30, p. 276].

## 5. Numerical results

### 5.1. Free-oscillation tests

We check the correctness of time integration program against the exact solutions of simple cases before doing numerical experiments for general cases. For this purpose we run the program without forcing/dissipation terms on the right-hand sides of (2.1) and (2.2). In the case of constant buoyancy parameter $N_0$, the numerical solutions of free oscillations are given by the normal modes presented in Section 3. Actually, we can derive the exact solutions of the system tailored to this particular difference formulation. Therefore, we

use those finite-difference normal mode eigenfunctions as the initial conditions for the time integrations. In order to maintain a close connection of this run with our previous study [17], the following parameter values are chosen:

$$
\begin{aligned}
&L_s = 50\ \text{km}, \quad L_x = L_y = 50\ \text{km in (2.15), so that } n = m,\\
&H_s = 5\ \text{km},\\
&T_s = (2\Omega)^{-1}, \quad \text{where } \Omega = \pi/(12\times 60\times 60)\ \text{s}^{-1},\\
&\Delta z = 1./J, \quad \text{where } J = 100 \text{ is the number of discrete cells,}\\
&N_0 = 5.0e-4\ \text{s}^{-1}, \quad \text{constant Brunt–Väisälä frequency,}\\
&\phi = 25^{\circ}N, \quad \text{latitude of coordinate center,}
\end{aligned}
\tag{5.1}
$$

together with $g = 9.8\ \text{m s}^{-2}$. The accuracy of numerical solutions depends on the choice of $\Delta z$ and $\Delta t$.

We run two cases. Fig. 2 shows the initial conditions of the first case corresponding to the vertical mode $k_i = 1$ of the first kind (IG) normal mode. There are four panels showing the vertical profiles of the variables plotted against $z$ from 0 to 1 in abscissa; (a) for the real part $U_r$ of $U$ by solid line, its imaginary part $U_i$ by dashed line, and the absolute value ABS(U) by thin solid line; (b)–(d), respectively, is same as (a), except for

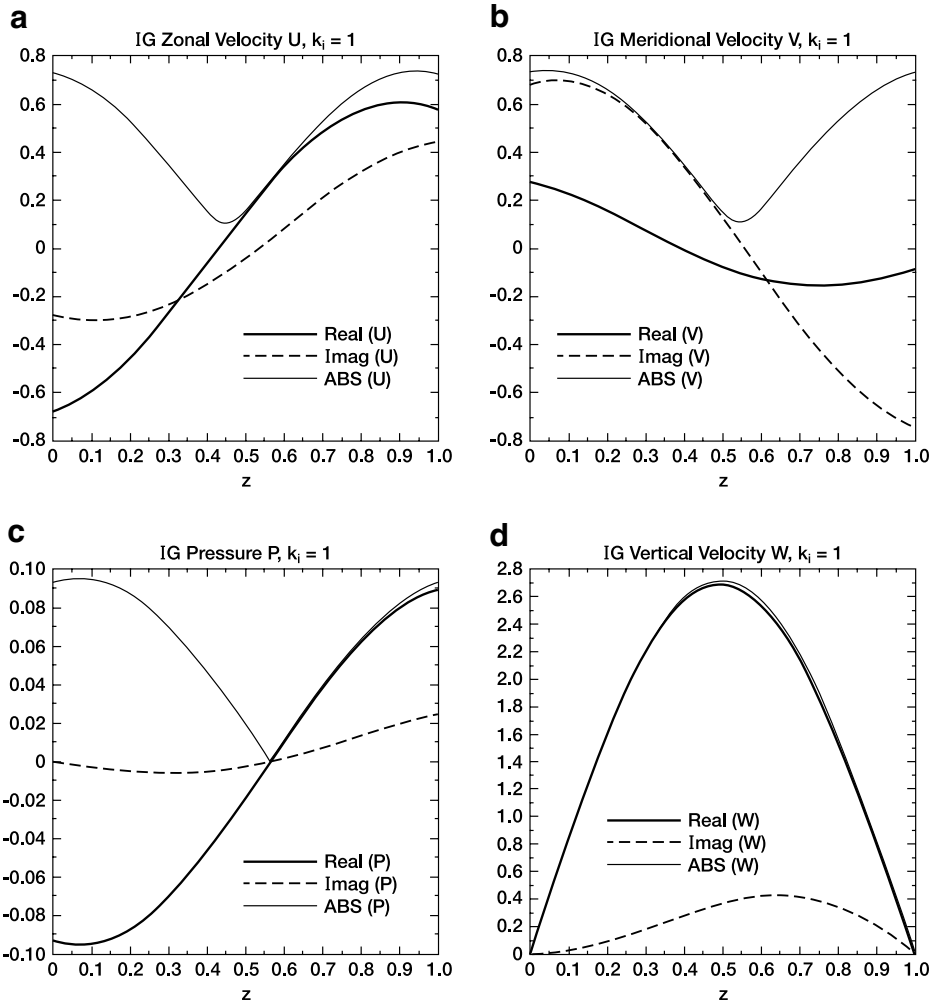


Fig. 2. Initial conditions with the IG-mode for vertical index $k_i = 1$. Solid lines are for the real part of variables, dashed lines for the imaginary part, and thin lines for the absolute value. (a) Zonal velocity $U$; (b) Meridional velocity $V$; (c) Pressure $P$; and (d) Vertical velocity $W$.

$V, W$ or $P$. The variable $S$ is not shown, since its profile is same as $W$ except for a proportional constant. Note that Fig. 2a is identical to Fig. 4a of [17], but the sign of the coefficient $A$ for the eigenfunctions is reversed.

Fig. 3 shows the initial conditions of the second case corresponding to the second kind (BII) normal mode, arranged in the same way as Fig. 2. However, we see large differences between Figs. 2 and 3. Because of the factor $\exp(ia_s\Gamma_2 z)$ in the eigenfuctions and a large value of $\Gamma_2$ in this case, the vertical variability of variables is large even for $k_i = 1$. Hence, we expect that the vertical truncation errors for the second case are considerably larger than those of the first case for the same space and time resolutions. The results of the two cases shown here are carried out with $J = 100$ and $\Delta t = 5$ min. The integrations are performed out to 1400 iterations, equivalent to 7000 min.

The gross check of calculations is done by computing the total energy product $\overline{TE}$ as defined by (2.12), which is now integrated horizontally.

$$\overline{TE} = |U_{j-1/2}|^2 + |V_{j-1/2}|^2 + a_s^2(|W_j|^2 + N^{-2}|S_j|^2). \tag{5.2}$$

By summing (5.2) with respect to the level index $j$ from 1 to $J$, we can define a measure of numerical error $E$ as

$$E = 1 - \sum_1^J (\overline{TE})\Delta z, \tag{5.3}$$

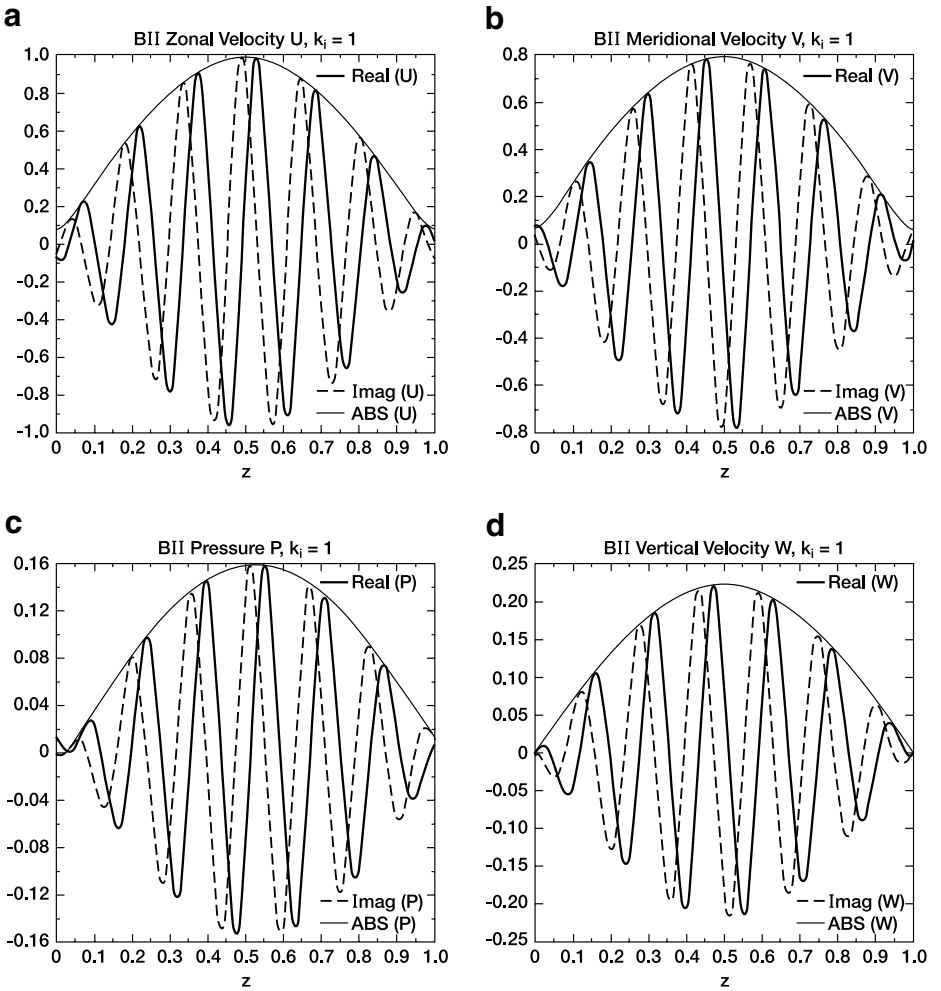


Fig. 3. Initial conditions with the BII-mode for vertical index $k_i = 1$. Notice striking differences between $U, V, P$ and $W$ of this figure and those shown in Fig. 2.

which should be zero for no error. The maximum of $E$ during the time integration is 1.0e−6 in the first case and 5.5e−3 in the second case. The errors are expected to be larger in the second case. Thus, the numerical scheme is considered to be sufficiently accurate, even though errors increase gradually in time.

Since the initial conditions are the finite-difference exact solutions, the results of time integrations should reproduce the oscillation of the normal mode with the expected eigenfrequency $\sigma$ in each case.

The real part of (2.14) at $x = y = 0$ is given by

$$\Re(u, v, w, p, s) = (U_r, -V_i, -W_i, P_r, S_r). \tag{5.4}$$

Thus, we get in the real parts as

$$\begin{aligned} &u = U_r = |\mathbf{V}| \cos\lambda, \quad v = -V_i = |\mathbf{V}| \sin\lambda, \\ &|\mathbf{V}| = (u^2 + v^2)^{1/2} = (U_r^2 + V_i^2)^{1/2}, \\ &\lambda = \tan^{-1}\left(\frac{-V_i}{U_r}\right). \end{aligned} \tag{5.5}$$

Fig. 4a shows the variation of flow angle $\lambda$ in degrees against time $t_i$ for the first case (IG mode) at the top level $z = 0.995$, where the velocity is largest. The unit of time $t_i$ here is the inertial period at $\phi = 25°$N which is 1703.66 min. The use of inertial period (28.394 h) as the unit of time becomes particularly convenient in the forcing case as seen later. The angle $\lambda$ decreases steadily starting from the initial value of 51.15°. This means that the velocity vector rotates clockwise. The computed period of rotation is 694.0 min ($t_i = 0.407$) against the exact value of 693.68 min. Thus, the rotation of velocity is reproduced accurately.

Fig. 4b shows the variation of $|\mathbf{V}|$ against time at the same level as in Fig. 4a. The magnitude starts from its maximum of 0.931 and decreases to its minimum of 0.391 after a quarter cycle. Then, it comes back to the maximum a half cycle later and repeats its oscillation. Thus, the period of velocity oscillation is one-half of that of the velocity rotation. This result can be verified from the exact solutions. At $x = y = 0$, the real part of the exact velocity components are expressed by

$$\begin{aligned} &\Re(u) = \overline{U}_r \cos(\sigma t) + \overline{U}_i \sin(\sigma t), \\ &\Re(v) = -\overline{V}_i \cos(\sigma t) + \overline{V}_r \sin(\sigma t). \end{aligned} \tag{5.6}$$

Here, $\overline{U}_r, \overline{U}_i, \overline{V}_r$ and $\overline{V}_i$ are the eigenfunctions of the velocity components used as the initial conditions, shown in Fig. 2a and b. By calculating the velocity magnitude $|\mathbf{V}| = (u^2 + v^2)^{1/2}$ from (5.6), we can show that the velocity magnitude oscillates with the frequency which is twice as large as $\sigma$.

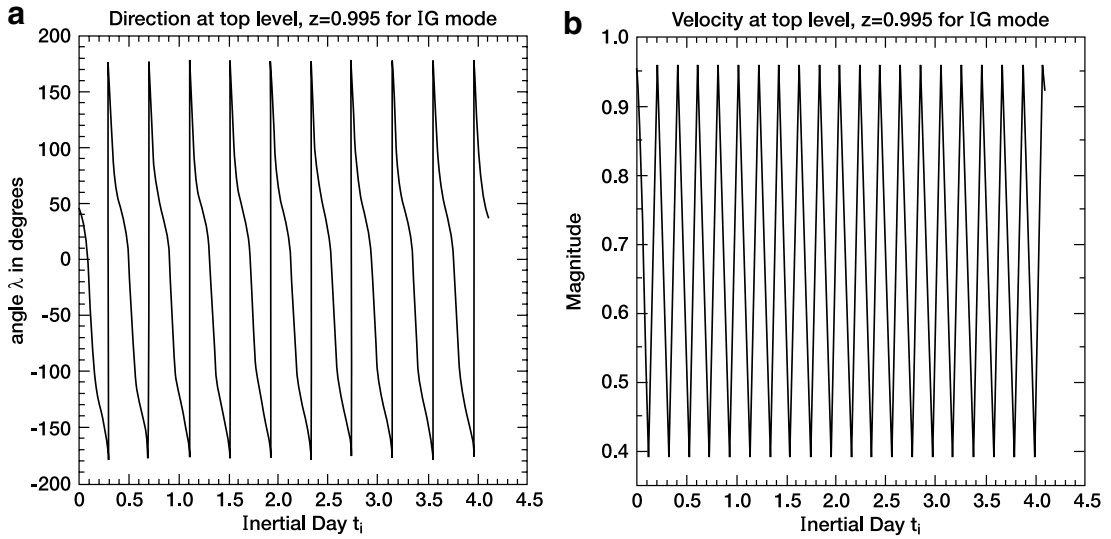


Fig. 4. (a) Direction, angle $\lambda$ in degrees, and (b) the magnitude of flow velocity at top level, $z = 0.995$ for the IG-mode initial conditions.

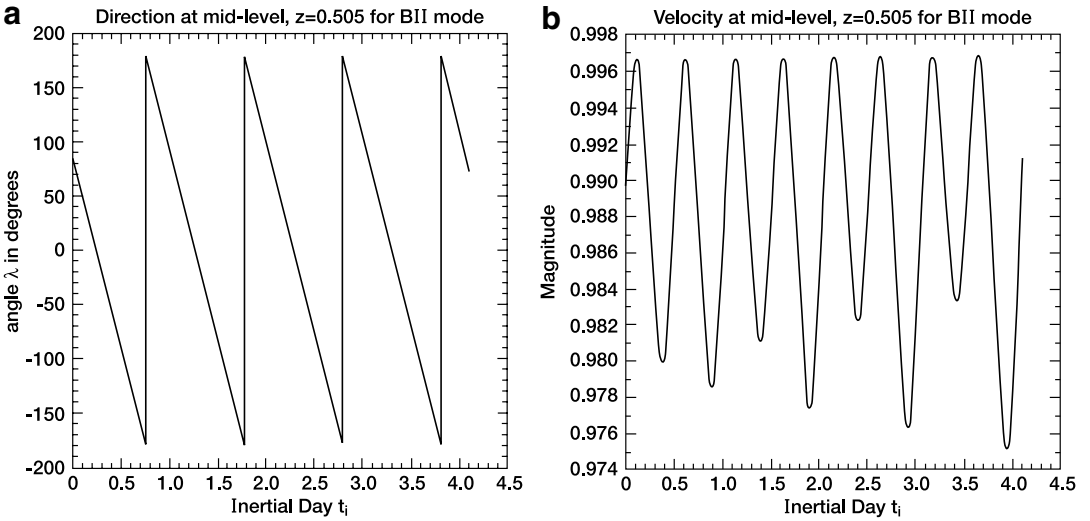


Fig. 5. (a) Direction, angle $\lambda$ in degrees, and (b) the magnitude of flow velocity at mid level, $z = 0.505$ for the BII-mode initial conditions.

Fig. 5a and b shows the same as Fig. 4a and b, except for the second case of the BII mode. These data, however, are taken at the mid-level $\Delta z = 0.505$, where the velocity is large. The variation of angle $\lambda$ in Fig. 5a shows a steady decrease of $\lambda$ from its initial value of 85.99°, which means a clockwise rotation. The computed period of rotation is 1731.7 min ($t_i = 1.016$) vs. the exact value of 1732.6 min. Hence, the velocity rotation is again reproduced very accurately. In contrast, we see in Fig. 5b that truncation errors of the velocity magnitude built up gradually in time. This is expected from the fact that the vertical structure of the BII mode is much finer than that of the IG mode. However, errors are still small on the order of 1.0e−3. Again we see that the period of velocity magnitude oscillation is one-half of that of the velocity rotation as expected from the exact solution.

In summary, when the normal mode functions are used as the initial conditions to the time integration of Eqs. (2.17)–(2.21) without dissipation, the normal mode profiles oscillate regularly (i.e. clockwise circular motion in the Northern Hemisphere) with the expected eigenfrequency and very little changes from the initial profiles. Truncation errors gradually built up as expected, but they are generally small. Without dissipation, the system can produce resonance [4, p. 285], when the time integration is performed with a specified forcing whose functional form and frequency match with those of a particular normal mode of the system. We have done such a resonance test to demonstrate that the total energy increases in proportion to $t^2$ when resonance occurs. In short, our overall tests indicate that the basic algorithm of time integration of Eqs. (2.17)–(2.21) is working satisfactorily. Next, we will present the results of forced oscillations.

### 5.2. Forced-oscillations

Pollard [27] investigated the generation of internal waves in the ocean by winds, which force the upper layer of the ocean, using a numerical version of the linear Boussinesq model. Price [28] used a multi-layer primitive-equation model to describe how the internal motions are developed by transient wind-forcing. Gill [12] also examined the behavior of internal waves in the ocean generated by moving storms using a linear, hydrostatic and incompressible model. Kundu and Thomson [19] considered a similar problem. While these investigators dealt with inviscid models, Kroll [18] added a viscous boundary layer near the top surface in the linear, hydrostatic and incompressible model to examine the propagation of wind-generated internal waves from the surface into the deep ocean. Crawford and Large [5] used a one-dimensional model of upper-ocean vertical mixing to investigate the ocean's response to storms over short (1–2 days) timescale.

In all of the above-mentioned studies and many others, one common objective is to understand the generation of internal waves of near-inertial frequency by atmospheric disturbances and how such waves propagate

downward into the deep ocean. Our objective here is same as above, but we include a complete effect of rotation in the forced problem. We also design the setup of model in such a way that the numerical results can be interpreted with the help of normal mode analyses. The numerical program is written to allow the variation of buoyancy parameter $N(z)$ and the eddy diffusivity $K(z)$ in height.

Concerning the mechanism of forcing the upper part of ocean (mixed layer) to generate waves, we assume that the system is at rest initially. Then, for $t > 0$, time-invariant wind stress components $F_x$ and $F_y$ at the top ($z = 1$) are specified as a forcing to the system. Here, we consider the following two configurations of forcing.

One type of forcing can be interpreted as the injection of the potential vorticity into the system [12]. The potential vorticity equation can be derived by taking the curl of the momentum equations (2.1) and (2.2) and using the continuity equation (2.4) and the buoyancy equation (2.5):

$$\frac{\partial}{\partial t}(pv) = \frac{\partial}{\partial z}\left(\frac{\partial F_y}{\partial x} - \frac{\partial F_x}{\partial y}\right), \tag{5.7}$$

where the potential vorticity, $pv$, is defined by

$$pv = \frac{\partial v}{\partial x} - \frac{\partial u}{\partial y} + f\frac{\partial}{\partial z}\left(\frac{s}{N^2}\right) + \frac{a_s\tilde{f}}{N^2}\frac{\partial s}{\partial y}. \tag{5.8}$$

The horizontal derivatives in $x$ and $y$ in (5.7) and (5.8) can be carried out using the expressions (2.14) and (2.16). Moreover, by integrating (5.7) with respect to time and horizontal space, we get the potential vorticity budget equation expressed in the vertical structure variables as

$$PV = \frac{\partial}{\partial z}\int_0^t (-m\widehat{F}_y - \mathrm{i}n\widehat{F}_x)\mathrm{d}t, \tag{5.9}$$

where the transformed potential vorticity is expressed by

$$PV = -mV - \mathrm{i}nU + f\frac{\partial}{\partial z}\left(\frac{S}{N^2}\right) + \mathrm{i}n\frac{a_s\tilde{f}}{N^2}S. \tag{5.10}$$

The right-hand side of (5.9) shows the forcing/dissipation of potential vorticity. In the case of no forcing/dissipation, such as free oscillations, the potential vorticity time tendency vanishes. (This property is used to check the accuracy of numerical program.) We designate this type of forcing as the vorticity forcing.

The other type of the forcing we consider may be interpreted as the injection of the divergence/convergence into the system. Kroll [18] postulates that the wind forcing produces a time-dependent viscous Ekman boundary layer at the surface which in turn forces the essentially inviscid interior by means of the vertical velocity (Ekman suction) in the boundary layer. Since the vertical resolution of our numerical model is too coarse to allow a well-defined Ekman boundary layer, we design a forcing formulation by simply specifying the divergence of the surface forcing vector $\mathbf{F}_s = (F_{x_s}, F_{ys})$. We designate this type of forcing as the divergence forcing.

The real part of the vorticity, $\mathrm{rot}\mathbf{F}_s$, or divergence, $\mathrm{div}\mathbf{F}_s$, of the surface forcing vector $\mathbf{F}_s$ can be expressed using (2.16) as

$$\mathrm{rot}\mathbf{F}_s = \Re\left(\frac{\partial F_{ys}}{\partial x} - \frac{\partial F_{xs}}{\partial y}\right) = (-m\widehat{F}_{ys,r} + n\widehat{F}_{xs,i})\cos\psi + (m\widehat{F}_{ys,i} + n\widehat{F}_{xs,r})\sin\psi, \tag{5.11}$$

where $\psi = mx + ny$. The additional subscripts r and i for $\widehat{F}_{xs}$ and $\widehat{F}_{ys}$ stand for their real and imaginary parts, respectively. Similarly,

$$\mathrm{div}\mathbf{F}_s = \Re\left(\frac{\partial F_{xs}}{\partial x} + \frac{\partial F_{ys}}{\partial y}\right) = (-m\widehat{F}_{xs,i} - n\widehat{F}_{ys,r})\cos\psi - (m\widehat{F}_{xs,r} - n\widehat{F}_{ys,i})\sin\psi. \tag{5.12}$$

The momentum fluxes $\widehat{F}_x$ and $\widehat{F}_y$ in (5.9) are defined by (2.16). We specify at $t = 0$ their surface ($z = 1$) values, $\widehat{F}_{xs}$ and $\widehat{F}_{ys}$, and hold them as constant for $t > 0$. We select the magnitudes of the real and imaginary parts of $\widehat{F}_{xs}$ and $\widehat{F}_{ys}$ to be all same which are equal to $\tau = 3.7818\mathrm{e}{-4}$ in dimensionless units. This value corresponds to the value of $2 \times \mathrm{e}{-3}\ \mathrm{m}^2\ \mathrm{s}^{-2}$, chosen by following the surface stress value given by Price [28]. Physically this forcing corresponds roughly to the wind speed of $10\ \mathrm{m\ s}^{-1}$. We select a small constant value of the vertical eddy diffusivity of $K = 1 \times \mathrm{e}{-7}\ \mathrm{m}^2\ \mathrm{s}^{-1}$, which makes the flow to be nearly inviscid.

In the following specific examples, we select two forcing cases. The first is the vorticity forcing case which is given by

$$\widehat{F}_{xs,r} = \tau, \quad \widehat{F}_{xs,i} = \tau, \quad \widehat{F}_{ys,r} = -\tau, \quad \widehat{F}_{ys,i} = \tau. \tag{5.13}$$

This specification with $m = n$ gives using (5.11) and (5.12) that

$$\mathrm{rot}\mathbf{F}_s = \tau(m+n)(\cos\psi + \sin\psi), \quad \mathrm{div}\mathbf{F}_s = 0. \tag{5.14}$$

Namely, the forcing term contains only vorticity and no divergence. The second is the divergence forcing case which is given by

$$\widehat{F}_{xs,r} = -\tau, \quad \widehat{F}_{xs,i} = -\tau, \quad \widehat{F}_{ys,r} = -\tau, \quad \widehat{F}_{ys,i} = \tau. \tag{5.15}$$

Similarly, this specification with $m = n$ gives

$$\mathrm{div}\mathbf{F}_s = \tau(m+n)(\cos\psi + \sin\psi), \quad \mathrm{rot}\mathbf{F}_s = 0. \tag{5.16}$$

Note that the divergence and vorticity forcing values are mutually exclusive.

The calculations are performed in complex arithmetic, but the real part of the solution is relevant as reality. The solutions are shown only at the coordinate center, $x = y = 0$. Moreover, the displayed numbers are in dimensionless unless otherwise mentioned. The values of the parameters are specified as in (5.1) of the free oscillation cases so that $J = 100$ and $\Delta t = 5$ min. The time integrations are performed out to 1440 iterations, equivalent to 7200 min.

### 5.2.1. Vorticity forcing case

Fig. 6 shows the evolution of the contours of zonal velocity component $u$ in height $z$ as the ordinate vs. inertial day $t_i$, whose unit is the inertial period of 28.394 h at this latitude. We notice the presence of two flow regimes. One is in the upper part of flow in the positive direction with an undulation having a near-inertial period, and the other in the lower part of flow in alternate sign having a somewhat shorter period than the inertial day. The appearance of $u$-pattern is in general agreement with the solutions obtained by Gill [12] and Kundu and Thomson [19]. The presence of two flow regimes is seen also in the $v$-contours, which are not shown. In order to demonstrate in a different way the contrast of flow features between the upper and lower parts of the $(z, t)$ domain, we show the next figure.

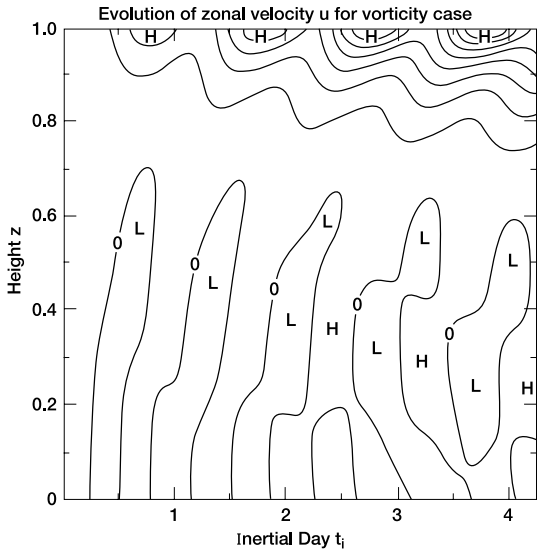


Fig. 6. Evolution of zonal velocity $u$ contours in height $z$ vs. inertial day $t_i$ for the vorticity forcing case. Range of values is $-0.01$ to $+0.17$ and contour interval is 0.02. Notice that the contours of the upper part are all positive, while the signs of values alternate in the lower part.

Fig. 7a shows the variation of flow angle $\lambda$ in degrees as defined in (5.5) vs. the inertial day $t_i$ at an upper level, $z = 0.905$, while Fig. 7b shows the velocity magnitude $|\mathbf{V}|$ against time $t_i$ at the same level. We see that the velocity of upper flow increases steadily with a near-inertial undulation. The direction of flow also undulates with the same period and tends to an asymptotic limit of near $-45°$ starting from the initial angle of 45°. Since the forcing is held constant in time, a forced steady flow will eventually be established as the result of Rossby adjustment process [31].

Fig. 8a and b shows the same as Fig. 7a and b, except at a typical lower level $z = 0.305$. A comparison of Figs. 7 and 8 demonstrates a clear distinction between the upper and lower flow regimes. The lower flow continues to rotate regularly clockwise starting from the initial angle of 45°. The period of rotation is shorter than the inertial day, but the period of rotation appears to increase slightly in time. On the other hand, the magnitude $|\mathbf{V}|$ of the low-level flow behaves in a more complex manner than that of the upper level. The period of velocity fluctuation is variable and much shorter compared with that of angle $\lambda$. This may indicate that the influence of steady flow has not yet arrived. (See the discussion of free-oscillations in Section 5.1.)

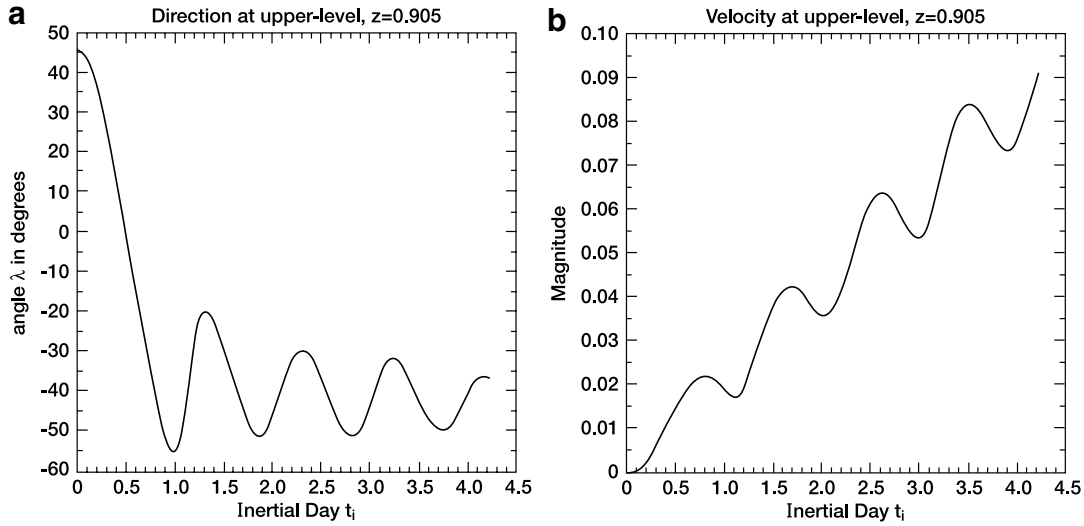


Fig. 7. (a) Direction, $\lambda$ and (b) the velocity of flow at an upper level, $z = 0.905$ for the vorticity forcing case.

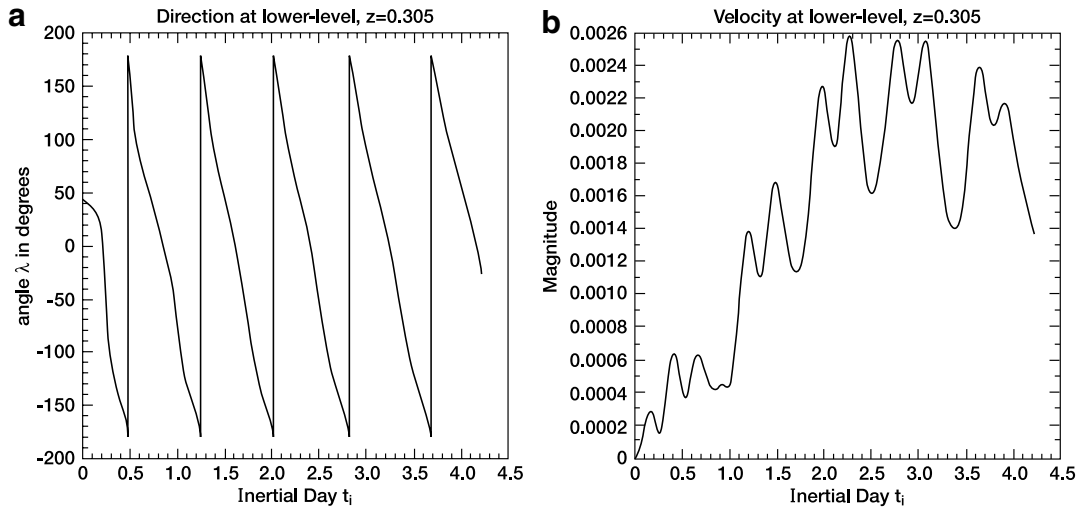


Fig. 8. (a) Direction, $\lambda$ and (b) the velocity of flow at a lower level, $z = 0.305$ for the vorticity forcing case.

The characteristic differences in the time evolutions of the flow angle and the velocity magnitude at the upper and lower levels shown in Figs. 7 and 8 are useful for interpreting the observation that the steady flow regime is developing in the upper part due to the forcing applied at the ocean surface, while transient flows still remain at the lower part as seen in Fig. 6. Moreover, the periods of resulting oscillations are near inertial in the upper part of the ocean despite the fact that the forcing is steady in time.

Note that the magnitude of horizontal velocity in Figs. 7b and 8b is dimensionless. To convert its unit dimensionally, we need to multiply it by 7.27 m $s^{-1}$ which is the scale factor in this case. Thus, the order of the upper flow velocity is 35 cm $s^{-1}$, while the order of the lower flow velocity is 1.5 cm $s^{-1}$. These numbers are in line of the observations of near-inertial waves in the ocean [27].

Regarding the development of vertical complexity in the flow due to a steady forcing, Fig. 9 shows the time evolution of the vertical velocity $w$ contours. The injection of positive vorticity at the top leads to a strong upwelling in the upper part of flow. The distinction between steady and transient flow regimes in Fig. 9 is not as clear as in Fig. 6, but the increase of vertical complexity of flow in time is noticeable. To examine the question of flow periodicity vs. vertical complexity quantitatively, we expand the vertical velocity solution spectrally in terms of the vertical normal mode functions (3.1) with (3.3).

The solution $W(z,t)$ can be expressed by

$$W(z,t) = \sum_i C_i(t) \sin(k_i \pi z) \exp(\mathrm{i} a_s \Gamma_2 z), \tag{5.17}$$

where $C_i(t)$ is the expansion coefficient as a function of time for vertical mode index $k_i$. The complex coefficient $C_i(t)$ is determined by the inversion process and we get

$$C_i(t) = 2 \int_0^1 W(z,t) \sin(k_i \pi z) \exp(-\mathrm{i} a_s \Gamma_2 z) \mathrm{d}z. \tag{5.18}$$

Note that there are two kinds of the inertio-gravity normal modes, IG and BII modes, so we need to calculate the coefficient separately for the two kinds. Also, we should mention that for evaluating the value of $\Gamma_2$ which is defined by (3.4) the value of $\sigma$ for a specific vertical mode index $k_i$ of either IG or BII mode must be used. In Table 1, instead of the $\sigma$'s of IG and BII modes, for convenience, we show their periods in hours and the ratios of these periods over the inertial period (28.394 h) of this case. The use of the normal mode frequencies in evaluating $\Gamma_2$ in (5.18) is important to properly specify the vertical expansion function, but it does not affect the evaluation of the periodicity of the coefficient $C_i(t)$.

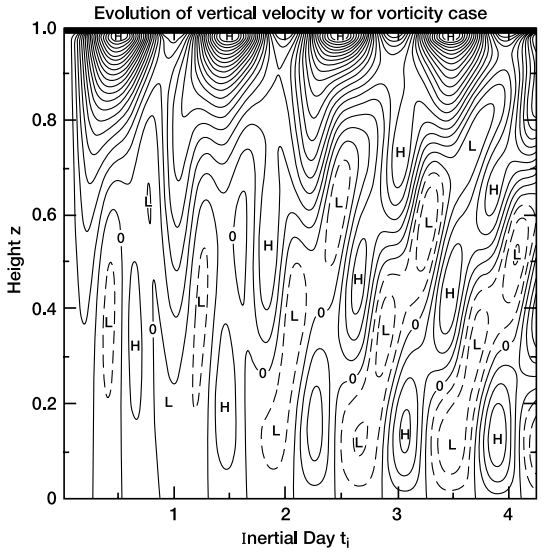


Fig. 9. Evolution of vertical velocity $w$ contours in height $z$ vs. inertial day $t_i$ for the vorticity forcing case. Range of values is −0.003 to +0.02 and contour interval is 0.001. Negative contours are dashed.

Table 1
Periods in hours and the ratio of period over the inertial period (IT) against the vertical mode index $k_i$ of the normal modes

| $k_i$ | IG (h) | IG/IT | BII (h) | BII/IT |
|---|---|---|---|---|
| 1 | 11.56127 | 0.40717 | 28.88771 | 1.01737 |
| 2 | 18.49632 | 0.65141 | 28.87900 | 1.01707 |
| 3 | 22.25864 | 0.78391 | 28.86577 | 1.01660 |
| 4 | 24.28165 | 0.85516 | 28.84947 | 1.01603 |
| 5 | 25.43968 | 0.89594 | 28.83147 | 1.01539 |
| 6 | 26.15117 | 0.92100 | 28.81285 | 1.01474 |
| 10 | 27.34049 | 0.96288 | 28.74378 | 1.01230 |
| 15 | 27.78571 | 0.97856 | 28.68007 | 1.01006 |
| 20 | 27.96619 | 0.98492 | 28.63700 | 1.00854 |

The first two entries are for the inertio-gravity (IG) modes and the other two entries for the boundary-induced inertial (BII) modes.

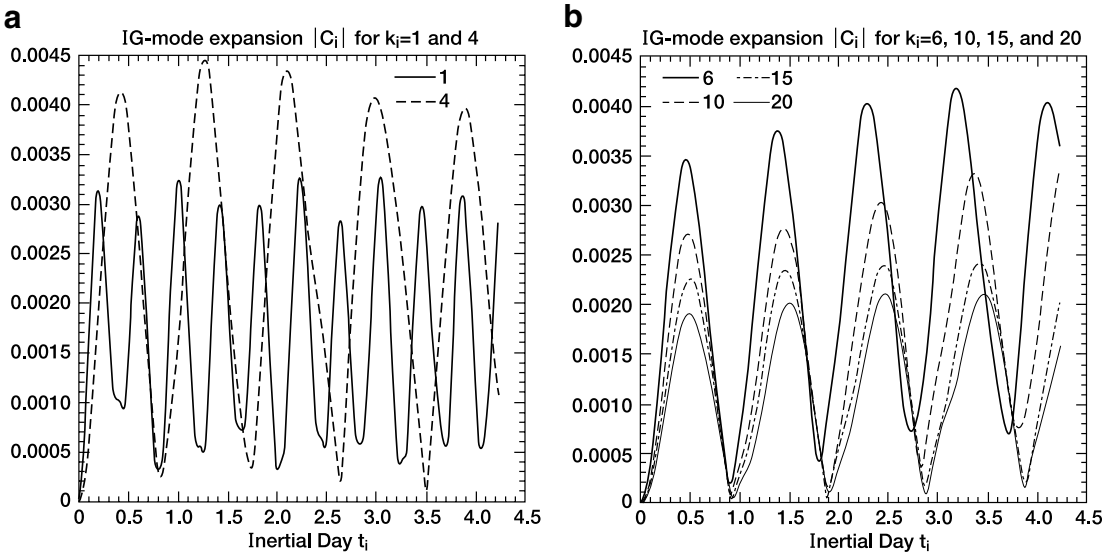


Fig. 10. Variation of $|C_i|$ against inertial day $t_i$ for IG-mode expansion in various vertical index $k_i$: (a) for $k_i = 1$ and 4, and (b) for $k_i = 6, 10, 15$ and 20.

Fig. 10 shows for the IG-mode the variation of absolute value of $C_i(t)$ against the inertial day for various values of $k_i$; (a) for $k_i = 1$ and 4; (b) for $k_i = 6, 10, 15$ and 20. The following two points are clearly noticeable. One finds in (a) that $|C_i|$ of $k_i = 4$ is larger than that of $k_i = 1$, but in (b) that $|C_i|$ decreases steadily as $k_i$ increases. Namely, the peak of $|C_i|$ appears around $i = 4$–6. Another important point is that each $|C_i|$ undergoes a clear oscillation with the period expected from that in Table 1 for a particular IG vertical mode $k_i$. For example, the $k_i = 1$ component oscillates with the period which is roughly 40% of inertial day, while the $k_i = 4$ component has the period about 85% of inertial day. Once the $k_i$ goes beyond 6, as seen in (b), the periods are close to one inertial day.

Fig. 11 shows the same as Fig. 10, except for the BII modes and (a) for $k_i = 1, 2, 3$ and 4. Unlike the projection onto the IG modes, the value of $|C_i|$ increases monotonically as $k_i$ increases. Because of this tendency the contribution of the BII modes becomes noticeable as $k_i$ increases in comparison to the contribution of the IG modes, even though the value of $|C_i|$ for lower $k_i$, as seen in Fig. 11a, is one order of magnitude smaller than that of the IG-modes (compare Figs. 10a and 11a). With respect to the periodicity of the oscillation of $|C_i|$, it is remarkable that the periods of oscillation for various $k_i$'s are all just about same and there is even a hint of the observation that the periods are even slightly larger than one inertial day as expected. We can emphasize here that the expansion procedure does not dictate the determination of the periods to match with

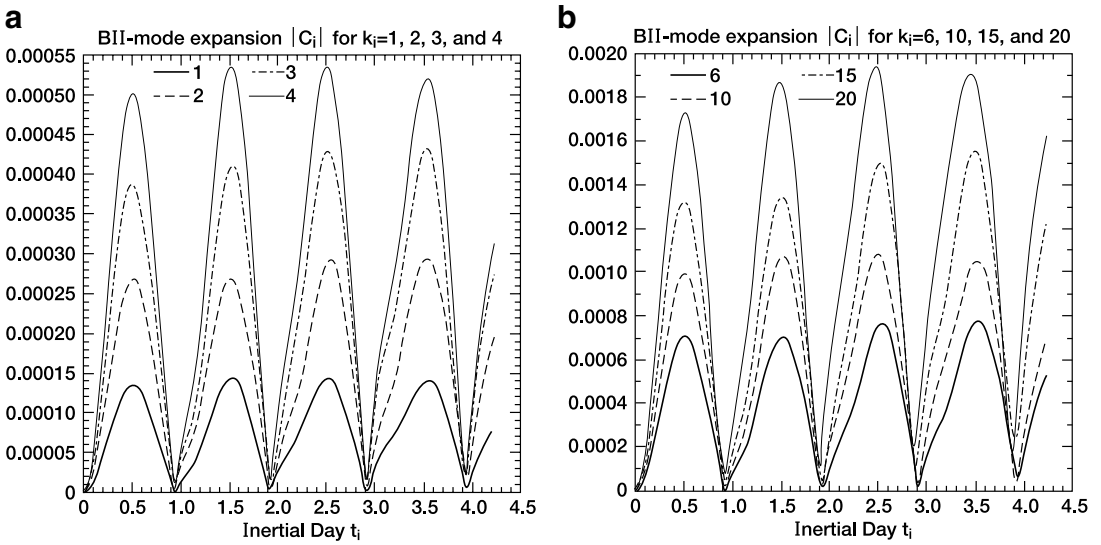


Fig. 11. Variation of $|C_i|$ against inertial day $t_i$ for BII-mode expansion in various vertical index $k_i$: (a) for $k_i = 1$–4, and (b) for $k_i = 6, 10, 15$ and 20.

those of the normal modes as seen in Table 1. Thus, the spectral analyses clearly demonstrate that the period of forced oscillation in this case is near inertial.

Now, we examine the role of the horizontal component of the Coriolis vector. The same program was run again by neglecting the $\tilde{f}$-terms. Fig. 12 shows the time evolution of the $u$-contours of this run. By comparing Fig. 12 with Fig. 6, in which the influence of $\tilde{f}$-terms is present, we notice that the separation of upper steady and lower transient flow regimes is more apparent without $\tilde{f}$-terms. Moreover, the overall $u$-contours of Fig. 12 are smoother and orderly than those of Fig. 6, though the ranges of contours are about same.

The above finding on the role of $\tilde{f}$-terms can be seen also from Fig. 13, which shows the spectral variation of $|C_i|$ of $w$ for the IG-mode from this run. By comparing Fig. 13 with Fig. 10, we notice that without the

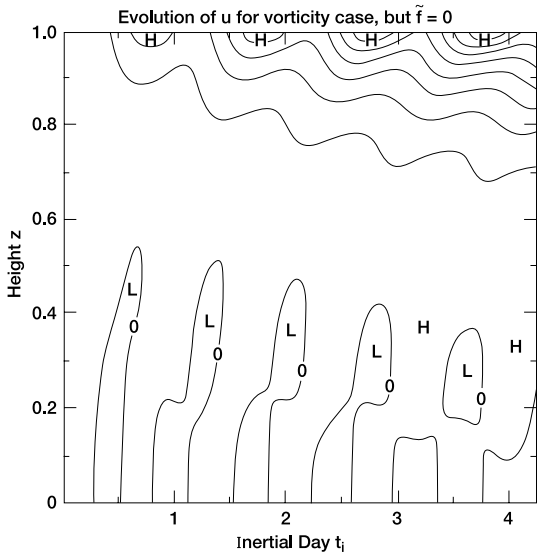


Fig. 12. Evolution of zonal velocity $u$ contours in height $z$ vs. inertial day $t_i$ for the vorticity forcing case without the $\tilde{f}$-terms. Range of values is $-0.01$ to $+0.17$ and contour interval is 0.02. Notice that the range of contours is almost identical to Fig. 6, but there is a subtle difference in the contour patterns between Figs. 6 and 12. See text.

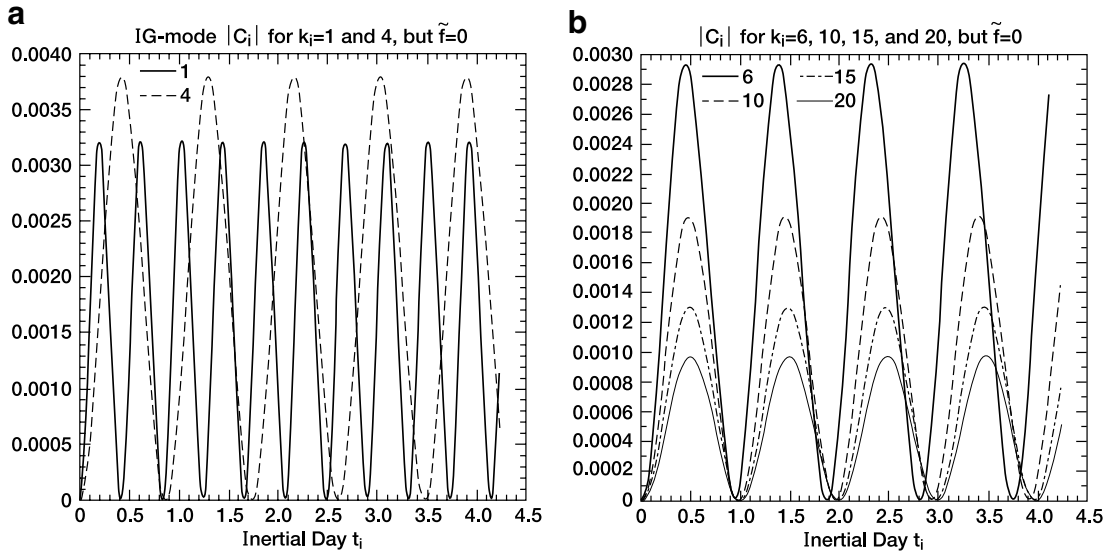


Fig. 13. Variation of $|C_i|$ against inertial day $t_i$ for IG-mode expansion like Fig. 10, but the $\tilde{f}$-terms are neglected in this vorticity forcing run.

$\tilde{f}$-terms the time evolution of $|C_i|$ is very regular and its magnitude is smaller in general and becomes much smaller in the higher $k_i$'s. For example, for $k_i = 20$ the value of $|C_i|$ without the role of $\tilde{f}$-terms becomes one half of the value with the $\tilde{f}$-terms. This means that the solutions tend to be rather orderly and smoother in the vertical.

### 5.2.2. Divergence forcing case

Next, we examine the difference in solutions due to the nature of forcing and consider the case of divergence forcing as specified by (5.15) and (5.16). Other than the forcing, everything else is the same with the vorticity

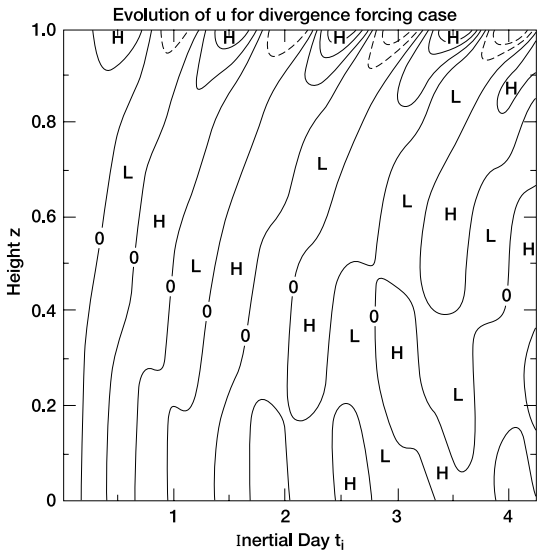


Fig. 14. Evolution of zonal velocity $u$ contours in height $z$ vs. inertial day $t_i$ for the divergence forcing case. Range of values is $-0.025$ to $+0.04$ and contour interval is 0.01. Negative contours are dashed. Notice that the signs of values alternate through out the entire depth unlike Fig. 6 of the vorticity run.

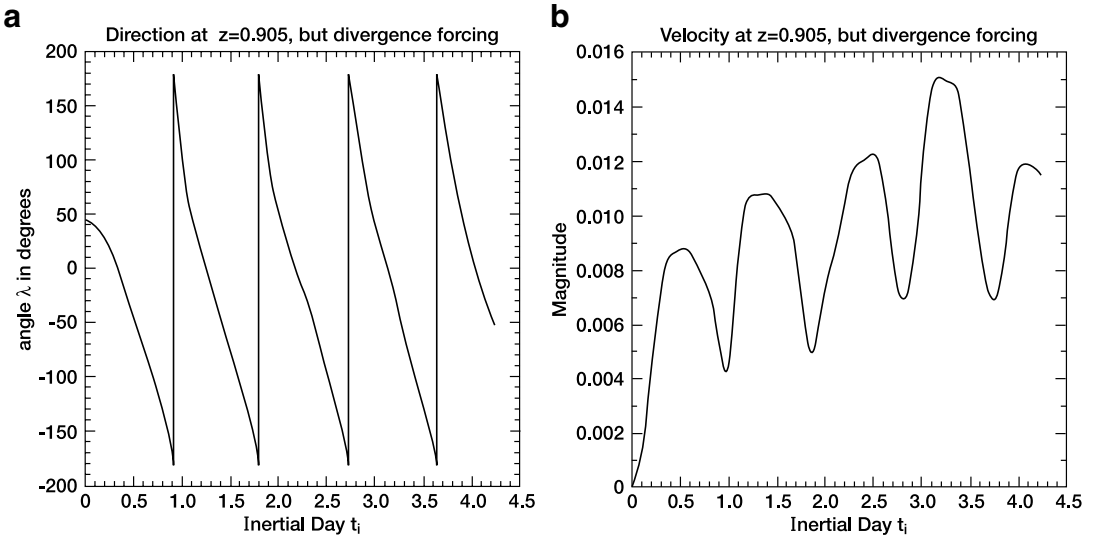


Fig. 15. (a) Direction, $\lambda$ and (b) the velocity of flow at an upper level, $z = 0.905$ just like Fig. 7, but this is the divergence forcing case.

run. However, as we will see, the solutions are very different in two cases. Fig. 14 shows the time-evolution of $u$-contours for the divergence forcing. By comparing Fig. 14 with Fig. 6 of the vorticity run, we immediately notice one remarkable difference that there is no clear separation of flow between the upper and lower parts, though the flow intensity is obviously larger near the top. The trough and ridge lines are slanted as the period of oscillation is close to one inertial day near the top and gradually becomes shorter downward.

Fig. 15 shows for (a) the direction and (b) the velocity of an upper flow at level $\Delta z = 0.905$ of the divergence run. By comparing Fig. 15 with Fig. 7 of the vorticity run, we see a marked difference in the flow at this level. We do not see the generation of steady solution and the flow oscillates with shorter period than one inertial day. In contrast, the time evolution of the direction and the velocity of flow at a lower level $\Delta z = 0.305$ (not shown) is similar to Fig. 8 of the vorticity run, indicating that the solutions are transient oscillations.

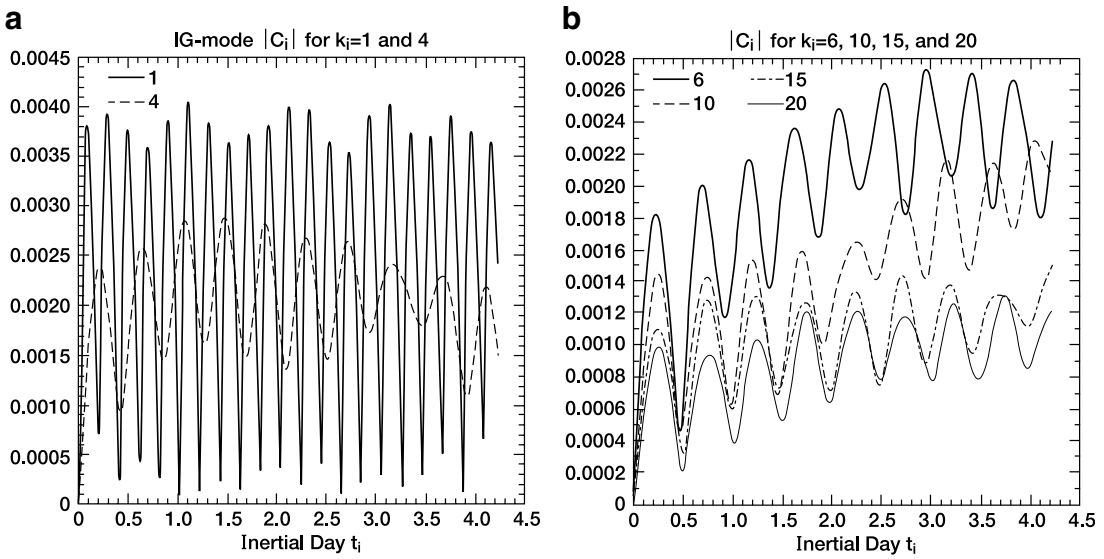


Fig. 16. Variation of $|C_i|$ against inertial day $t_i$ for IG-mode expansion in various vertical index $k_i$ just like Fig. 10, but this is the divergence forcing case.

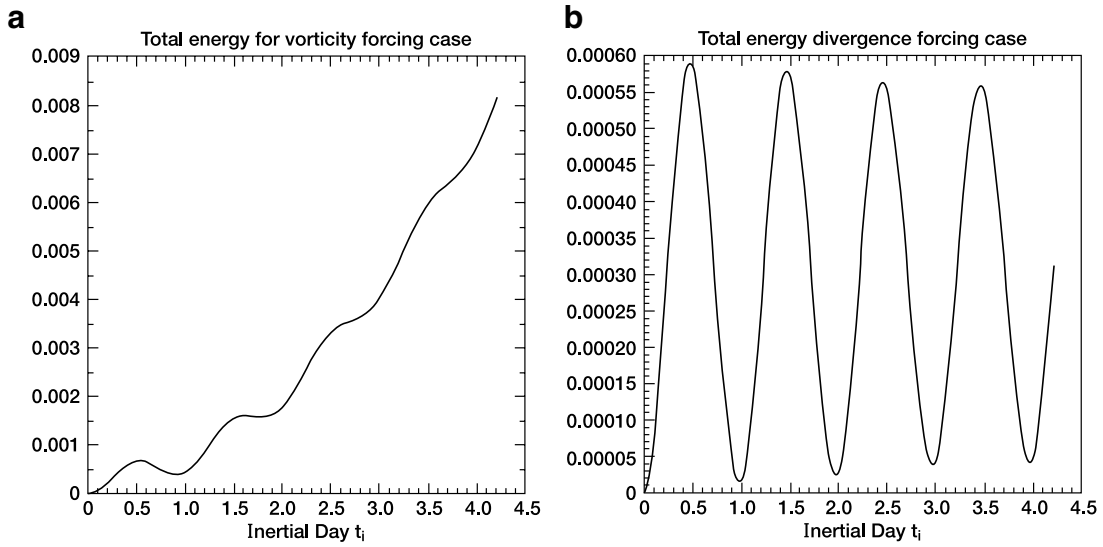


Fig. 17. Variation of total energy which is the vertically integrated $\overline{TE}$ as defined by (5.2) against inertial day; (a) the vorticity forcing case and (b) the divergence forcing case.

To support the finding that there are no steady solutions in the divergence forcing case, it is illuminating to show the spectral behavior of the normal mode expansion coefficient $|C_i|$ of the $w$-field. Fig. 16 shows the same as Fig. 10 for (a) $k_i = 1$ and 4, and (b) for $k_i = 6, 10, 15$ and 20 of the IG mode, except for the divergence forcing case. In comparing Figs. 10a and 16a, while the magnitudes are about same, we see that the periods of oscillations are very different. It is of interest to observe that the period of oscillation of the $k_i = 1$ mode is almost identical to that of the $k_i = 1$ normal mode oscillation of velocity shown in Fig. 4b. We recall that the magnitude of normal mode velocity oscillates with the frequency twice as large as $\sigma$.

Another evidence for the fact that the divergence forcing does not generate steady solutions contrary to the vorticity forcing may be seen in Fig. 17. It shows the evolution of the vertically integrated total energy product $\overline{TE}$ as defined by (2.12) or (5.2) against inertial day: (a) for the vorticity forcing case, and (b) for the divergence forcing case. Note a marked difference between the two cases. The total energy of the vorticity case is one order of magnitude larger than that of the divergence case and almost monotonically increased with time. In contrast, in the divergence case the total energy simply oscillated rather regularly with the period close to one inertial day. Actually, even in the vorticity forcing case we notice a small-amplitude oscillation, superimposed on a monotonically increasing curve, and the magnitude of its amplitude is on the order of that of the divergence case. Therefore, it seems apparent that the total energy of the vorticity case consists of the sum of the energy of transient and steady motions, while in the divergence case the total energy consists of only transient motions. As seen from (2.11) the total energy should balance with the accumulated total work done by the forcing. The order of magnitude of the calculated imbalance is less than 0.1%. This indicates the gross check of calculations is satisfactory in both cases. A similar check was made to verify that the total energy is unaffected by the presence of the non-traditional effect.

Lastly, we should comment on the influence of $\tilde{f}$-terms in the divergence forcing case. We have compared the results from the two runs of the divergence forcing case with and without the $\tilde{f}$-terms. Since there are no new additional features in the role of $\tilde{f}$-terms in this case other than we already found from the vorticity forcing case, we will not discuss any detail of the results. However, we should mention that one common feature stands out between the vorticity and divergence forcing cases concerning the role of $\tilde{f}$-terms. Namely, with the presence of $\tilde{f}$-terms the inertio-gravity oscillations become more intense and less regular in both cases. Increased intensity and decreased regularity in the solutions come from the contribution of the additional kind (BII mode) of the inertio-gravity oscillations. The magnitude of the difference in the solutions with and without the $\tilde{f}$-terms depends on the structure of forcing. When more forcing is projected on the BII mode, more

intensity and complexity may appear to increase in the solution as suggested from the spectral analysis of the normal mode expansion coefficient $|C_i|$.

## 6. Conclusions and additional comments

The numerical program described here is one of the simplest non-trivial ones to study the inertio-gravity oscillations including the complete effects of rotation. Yet, the program is versatile to handle the temporal evolutions of a variety of free and forced oscillations under specified initial and forced conditions. As a demonstration of experiments, we selected the cases of constant buoyancy parameter $N$ and a negligibly small value of the eddy diffusivity $K$, whereby numerical results can be compared with analytical solutions and/or interpreted in light of the normal mode solutions.

For example, the use of normal mode solutions as the initial conditions for free oscillations provided a powerful means to check the accuracy of numerical calculations. Also, the initial-value approach gives an easy visualization of motions described by the solutions from the eigenvalue approach. Thus, two are synergistic and helpful to understand the role of unfamiliar boundary-induced inertial (BII) mode together with the traditional inertio-gravity (IG) mode when the complete rotation effects are included.

Speaking on the role of the BII mode, the author was struck by the statement in [9] that "it does seem that the 'near-inertial' band of waves with a frequency close to $f$ does have different characteristics from the rest of the frequency spectrum." Garrett [9] is referring to the well-known observation in oceanography that the near-inertial currents are ubiquitous and prominent, though intermittent [23]. Hence, we set up an example of forced oscillations which simulates the generation of near-inertial motions by *steady* wind stress applied at the top of model ocean and investigated the role of the BII mode in conjunction with the IG mode. The parameter values used in this example such as in (5.1) are in line of those adapted in many numerical experiments of near-inertial oscillations in the ocean [1,12,18,19,28].

It is useful to distinguish two types of wind–stress forcing by separating it into the vorticity and divergence components. As far as we are aware, such a practice has not been reported in the literature of near-inertial oscillations. In fact, in the case of vorticity forcing steady undulating motions develop in the upper part of the ocean and fluctuate with the period very close to one inertial day. The upper steady undulating motions gradually move downward to a deeper depth where transient oscillations with the period shorter than one inertial day occupy. In contrast, the divergence forcing generates only transient oscillations with variable periods in depth which are smaller than one inertial period. In both cases, the periods of oscillations in the upper part are near inertial and become shorter gradually downward.

The observation that the wind forcing may generate near-inertial oscillations in the ocean has been explained more or less in many works e.g. [12,19]. The unique aspects of the present findings are twofold. One is the type of wind forcing. It is the rotational wind rather than the irrotational wind forcing which is responsible to generate steady forced currents. The other is the additional physics coming from the consideration of complete rotation effect. The fact that the axis of rotation is not parallel with the gravity, except at the poles, together with the presence of boundary at the bottom creates two kinds of inertio-gravity (IG and BII) waves. Depending on the vertical structure of forcing, the projection of forcing onto the IG and BII modes differs. The type of wind-forcing applied at the ocean surface only does not particularly favor the generation of the BII waves. One can design a particular initial condition or a forcing mechanism which produces a favorable response to the BII mode as done in [1].

Regardless the nature of forcing at the top, it appears that the effect of steady prescribed force at the top overwhelms the pressure gradient force in the shallow upper layer. Thus, the period of the internal gravity waves under rotation generated by surface forcing is predominantly near inertial. The $\tilde{f}$-terms play little role in the upper part of flow for determining the period of near-inertial oscillations generated by steady wind–stress forcing, but details of the morphology of inertio-gravity oscillations as a whole are noticeably affected by the $\tilde{f}$-terms.

Additional comments will be made concerning the role the $\tilde{f}$-terms. In the present numerical experiments we assumed that the buoyancy parameter $N$ is constant. As investigated numerically in our earlier work [17] and analytically by Gerkema and Shrira [11], the vertical variation of $N$ has a unique impact on details of the inertio-gravity wave solutions with the $\tilde{f}$-terms. Actually, we have made model runs using two different forms

of the vertical distribution of $N$; one is the exponential form of Garrett and Munk [10] and the other is the form given in Vlasenko et al. [37, p. 37]. We have not finished the compilation of the results yet, but this is a kind of numerical experiments expected to be carried out by this model.

Another parameter which can be varied in the model is the eddy diffusivity coefficient $K$. We used a very small value of $K$ so that the model is essentially inviscid. For a realistic case study, it is likely that the vertical dependence of the value of $K$ matters. However, it is doubtful that a mere specification of the value of $K$ renders a meaningful replacement to the action of turbulent flow. Rather it is an intriguing thought of investigating the non-linear interaction between the two different kinds (IG and BII) of inertio-gravity modes, just like an idea of the spontaneous generation of inertial-gravity waves resulting from non-linear interactions among various large-scale motions addressed in [40].

The last point which we add here is the question of in which geographical area the non-traditional effect is most effective. Qualitative arguments to this question based on scale analyses e.g. [3,38] point out that the equatorial region is likely most affected by the traditional approximation. A satisfactory answer to this question will be given, if we had the theory of free oscillations of deep non-hydrostatic rotating fluid contained in a spherical shell without the traditional approximation. Despite the fact that there is an extensive literature on such a theory from the standpoint of geophysical fluid dynamics e.g. [13], we are not aware of any specific study which throws a light on this question. Recently, Thuburn et al. [34] and Kasahara [16] investigated numerically the normal modes of deep global atmospheres with a specific intention to detect the presence of a unique mode which may correspond to the BII mode. Unfortunately, these studies could not confirm the presence of any new mode beside the normal modes which are already known. It is speculated that the detection of a new mode may require a high vertical grid resolution in their numerical schemes as we know that the BII eigenfuctions can be highly variable in the vertical. Thus, the definitive answer to the question regarding the role of $\tilde{f}$-terms on the sphere remains to be seen.

## Acknowledgments

The author wishes to thank John Gary who has contributed during the early phase of this work, read the first draft, and gave him useful comments. Also, the author thanks William Large who introduced him into the subject of near-inertial oscillations in the sea and Joseph Tribbia for his interest and advice during this work. Two anonymous reviewers made constructive comments to improve the readability of this article for which the author is very grateful.

## Appendix

The following basic quantities are used to scale the variables and parameters in dimensionless form:

Length scale $L_s$; Depth scale $H_s$; Time scale $T_s = (2\Omega)^{-1}$,
Horizontal velocity components; $U_s = L_s/T_s$,
Vertical velocity component; $W_s = H_s/T_s$.

The original dimensioned quantities, appeared on the right-hand sides, are denoted by prime superscript. The dimensionless quantities on the left-hand sides are scaled as follows:

$$(x,y) = (x',y')L_s^{-1}, \quad z = z'H_s^{-1}, \quad t = t'T_s^{-1},$$
$$(u,v) = (u',v')U_s^{-1}, \quad w = w'W_s^{-1}, \quad p = p'U_s^{-2}, \quad s = s'T_sW_s^{-1},$$
$$(F_x,F_y) = (F'_x,F'_y)T_sH_s^{-1}U_s^{-1},$$
$$f = f'T_s = \sin\phi, \quad \tilde{f} = \tilde{f}'T_s = \cos\phi.$$

Diffusivity coefficient: $K = K'T_sH_s^{-2}$,
Brunt–Väisälä frequency: $N = N'T_s$.

## References


[1] A. Beckmann, S. Diebels, Effects of the horizontal component of the earth's rotation on wave propagation on an f-plane, Geophys. Astrophys. Fluid Dyn. 76 (1994) 95–119.
[2] L.M. Brekhovskikh, V. Goncharov, Mechanics of Continua and Wave Dynamics, Springer-Verlag, 1985.
[3] A. Colin de Verdière, R. Schopp, Flows in a rotating spherical shell: the equatorial case, J. Fluid Mech. 276 (1994) 233–260.
[4] R. Courant, D. Hilbert, Methods of Mathematical Physics, Vol. 1, Interscience Pub., 1953.
[5] G.B. Crawford, W.G. Large, A numerical investigation of resonant inertial response of the ocean to wind forcing, J. Phys. Oceanogr. 26 (1996) 873–891.
[6] T. Davies, M.J.P. Cullen, A.J. Malcolm, M.H. Mawson, A. Staniforth, A.A. White, N. Wood, A new dynamical core for the Met Office's global and regional modelling of the atmosphere, Q. J. R. Meteorol. Soc. 131 (2005) 1759–1782.
[7] D.R. Durran, C. Bretherton, Comments on "The roles of the horizontal component of the earth's angular velocity in nonhydrostatic linear models", J. Atmos. Sci. 61 (2004) 1982–1986.
[8] C. Eckart, Hydrodynamics of Oceans and Atmospheres, Pergamon Press, 1960.
[9] C. Garrett, What is the "near-inertial" band and why is it different from the rest of the internal wave spectrum? J. Phys. Oceanogr. 31 (2001) 962–971.
[10] C. Garrett, W. Munk, Space–time scales of internal waves, Geophys. Fluid Dyn. 3 (1972) 225–264.
[11] T. Gerkema, V.I. Shrira, Near-inertial waves in the ocean: beyond the 'traditional approximation', J. Fluid Mech. 529 (2005) 195–219.
[12] A.E. Gill, On the behavior of internal waves in the wakes of storms, J. Phys. Oceanogr. 14 (1984) 1129–1151.
[13] H.P. Greenspan, The Theory of Rotating Fluids, Cambridge University Press, 1969.
[14] A. Kasahara, The roles of the horizontal component of the earth's angular velocity in nonhydrostatic linear models, J. Atmos. Sci. 60 (2003) 1085–1095.
[15] A. Kasahara, On the nonhydrostatic atmospheric models with inclusion of the horizontal component of the earth's angular velocity, J. Meteorol. Soc. Jpn. 81 (2003) 935–950.
[16] A. Kasahara, Free oscillations of deep nonhydrostatic global atmospheres: theory and a test of numerical schemes, NCAR Tech. Note TN-457+STA, 2004. Available from http://www.ucar.edu/communications/technotes/.
[17] A. Kasahara, J.M. Gary, Normal modes of an incompressible and stratified fluid model including the vertical and horizontal components of coriolis force, Tellus 58A (2006) 368–384.
[18] J. Kroll, The propagation of wind-generated inertial oscillations from the surface into the deep ocean, J. Marine Res. 33 (1975) 15–51.
[19] P.K. Kundu, R.E. Thomson, Inertial oscillations due to a moving front, J. Phys. Oceanogr. 15 (1985) 1076–1084.
[20] P.H. LeBlond, L.A. Mysak, Waves in the Ocean, Elsevier, 1978.
[21] J. Marshall, C. Hill, L. Perelman, A. Adcroft, Hydrostatic, quasi-hydrostatic, and nonhydrostatic ocean modeling, J. Geophys. Res. 102 (C3) (1997) 5733–5752.
[22] Yu Z. Miropol'sky, O.D. Shishkina, Dynamics of Internal Gravity Waves in the Ocean, Kluwer Academic Pub., 2001.
[23] W. Munk, N.A. Phillips, Coherence and band structure of inertial motions in the sea, Rev. Geophys. 6 (1968) 447–472.
[24] N.A. Phillips, The equations of motion for a shallow rotating atmosphere and the traditional approximation, J. Atmos. Sci. 23 (1966) 626–628.
[25] N.A. Phillips, Reply, J. Atmos. Sci. 25 (1968) 1155–1157.
[26] N.A. Phillips, Dispersion Processes in Large-Scale Weather Prediction, WMO 700, World Meteorol. Organi., 1990.
[27] R.T. Pollard, On the generation by winds of inertial waves in the ocean, Deep-Sea Res. 17 (1970) 795–812.
[28] J.F. Price, Internal wave wake of a moving storm. Part I: scales, energy budget and observations, J. Phys. Oceanogr. 13 (1983) 949–965.
[29] L.F. Richardson, Weather Prediction by Numerical Process, Cambridge University Press, 1922 (Reprint by Dover Pub., 1965).
[30] R.D. Richtmyer, K.W. Morton, Difference Methods for Initial-Value Problems, Interscience Pub., 1967.
[31] C.-G. Rossby, On the mutual adjustment of pressure and velocity distributions in certain simple current system, II, J. Marine Res. 1 (1937–38) 239–263.
[32] B. Saint-Guily, On internal waves. Effects of the horizontal component of the earth's rotation and of a uniform current, Deut. Hydrograph. Zeit. 23 (1970) 16–23.
[33] M.E. Stern, Ocean Circulation Physics, Academic Press, Berlin, 1975.
[34] J. Thuburn, N. Wood, A. Staniforth, Normal modes of deep atmospheres. I: spherical geometry, Q. J. R. Meteorol. Soc. 128 (2002) 1771–1792.
[35] J. Thuburn, N. Wood, A. Staniforth, Normal modes of deep atmospheres. II: f–F plane geometry, Q. J. R. Meteorol. Soc. 128 (2002) 1793–1806.
[36] G. Veronis, Comments on Phillips' proposed simplification of the equations of motion for a shallow rotating atmosphere, J. Atmos. Sci. 25 (1968) 1154–1155.
[37] V. Vlasenko, N. Stashchuk, K. Hutter, Baroclinic Tides, Cambridge University Press, 2005.
[38] A.A. White, R.A. Bromley, Dynamically consistent quasi-hydrostatic equations for global models with a complete representation of the Coriolis force, Q. J. R. Meteorol. Soc. 121 (1995) 399–418.
[39] A.A. White, B.J. Hoskins, I. Roulstone, A. Staniforth, Consistent approximate models of the global atmosphere: shallow, deep, hydrostatic, quasi-hydrostatic and non-hydrostatic, Q. J. R. Meteorol. Soc. 131 (2005) 2081–2107.
[40] P.D. Williams, P.L. Read, T.W.N. Haine, Spontaneous generation and impact of inertia-gravity waves in a stratified, two-layer shear flow, Geophys. Res. Lett. 30 (24) (2003) 2255, doi:10.1029/2003GL018498.